Results on Total and Elastic Cross Sections in Proton–Proton Collisions at $\sqrt{s} = 200\ GeV$ Obtained with the STAR Detector at RHIC

Włodek Guryn and Bogdan Pawlik

December 6, 2018

Abstract

We report the results on the total and elastic cross sections in proton-proton collisions at the Relativistic Heavy Ion Collider (RHIC) at $\sqrt{s} = 200\ GeV$. The results were obtained with the Roman Pot setup of the STAR experiment at the Relativistic Heavy Ion Collider (RHIC). The setup was used to measure elastic differential cross section in the four–momentum transfer squared (t) range $0.045 \leq -t \leq 0.14$ (GeV/c)^2. Elastic scattering was detected in the Roman Pot system, which was operated during standard data collection at STAR at the distance of about $8\sigma_y$ from the beam, where σ_y is the beam gaussian width in the vertical coordinate. The results include the value of the exponential slope parameter B of the elastic differential cross section $d\sigma/dt$ in the measured small $-t$ range and the total cross section σ_{tot} obtained from the extrapolation of the $d\sigma/dt$ to the optical point at $-t = 0$ (GeV/c)^2. We also present the value of elastic cross section σ_{el}. All results are compared with the world data.

Revision : 1.50

Contents

1 Introduction

Revision : 1.28

The special role of the elastic channel in proton–proton (pp)scattering at high energies is evident by the fact that it contributes almost 20%, see Fig. 3b, of the total cross section at the highest energies, at which the elastic scattering was measured. This, coupled with the importance of understanding the diffraction process, not only as the shadow of the many inelastic channels present at high energies, but also in terms of basic concepts related to QCD, has made nucleon-nucleon elastic scattering one of the most studied reactions in high energy physics. By using perturbative approach, the accepted theory of strong interactions, Quantum Chromo Dynamics (QCD), has been very successful in describing hadronic interactions at large four-momentum-transfer squared $|t|$. For small $|t|$-values of elastic scattering, the theory has not been as successful. This is the regime of soft hadronic interactions where phenomenological models, constrained by asymptotic theorems, are used to explain the nature of the hadronic interaction.

The special role of the elastic amplitude is often viewed in terms of the optical theorem, Eq. 8, as a shadow of the many inelastic channels present at high energies. By measuring the energy dependence of pp–total cross-section, σ_{tot}, in an uncovered yet domain of energies at RHIC one adds to the understanding of the phenomenology of this basic scattering process.

The summary of elastic scattering measurements and phenomenological models is given in [1, 2], we shall mention only a few questions here. The pp total cross sections measured at Serpukhov and the Intersecting Storage Rings (ISR) at CERN in the 1970s were found to rise with energy. Until then it was generally accepted that the total cross sections for both pp and $p\bar{p}$ would decrease as a function of *cms* energy and converge to a common constant value. The $\log^2 s$ behavior versus $\log\ s$ behavior of the rise of σ_{tot} is still an important topic for investigation.

From general considerations of unitarity and analyticity, the difference in the total pp and $p\bar{p}$ cross section is predicted to converge to zero at large values of s,

$$\frac{\sigma_{tot}(p\bar{p})}{\sigma_{tot}(pp)} \to 1, \tag{1}$$

and the rate at which the pp total cross section rises is limited by the Froissart bound,

$$\sigma_{tot}(s) < \frac{1}{m_\pi^2} \log^2 s. \tag{2}$$

Also, the σ_{tot} measurements at RHIC are important since there are no measurements of σ_{tot} between the ISR energies and the measurements at the LHC energies [5] in the TeV range. Furthermore, RHIC $\sqrt{s}$ range is still where one can expect a measurable difference between pp and $p\bar{p}$ total cross sections.

The elastic scattering of protons Fig. 1 is described by a scattering amplitude which has two components: the electromagnetic part, described by the well-known Coulomb amplitude f_c, and the hadronic part, described by the hadronic amplitude f_h. The amplitudes are a function of *cms* energy $\sqrt{s}$ and four-momentum-transfer squared $|t|$. The differential elastic pp cross section can be expressed as a square of the scattering

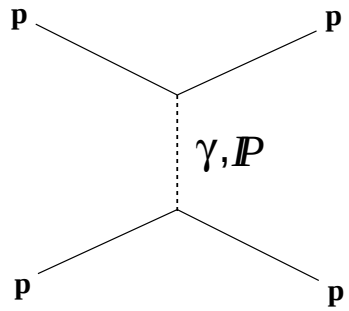

Figure 1: Diagram of elastic scattering.

amplitude:

$$\frac{d\sigma_{el}}{dt} = \pi |f_c + f_h|^2. \tag{3}$$

The spin independent hadronic amplitude f_h is usually parameterized as:

$$f_h = \left(\frac{\sigma_{tot}}{4\pi}\right)(\rho + i)\exp\left(-\frac{1}{2}B|t|\right). \tag{4}$$

The quantity ρ is the ratio of the real to imaginary part of the nuclear amplitude at $|t| = 0$ and is related to the high-energy behavior of the total cross section via dispersion relations. This means that ρ is related to the behavior of the total cross section σ_{tot} at higher energies. The Coulomb amplitude f_c is given by:

$$f_c = -\frac{2\alpha G^2(t)}{|t|}\exp(i\alpha\phi), \tag{5}$$

where α is the fine structure constant, $G(t)$, is the proton electromagnetic form factor, and ϕ is the Coulomb phase, which is:

$$\phi = ln\left(\frac{0.08}{|t|}\right) - 0.577. \tag{6}$$

Thus, the differential cross section $\mathrm{d}\sigma/\mathrm{d}t$ for elastic scattering in the forward angle region is determined by Coulomb and nuclear amplitudes and the interference term between them. The cross section is given by (see for example Ref. [3])

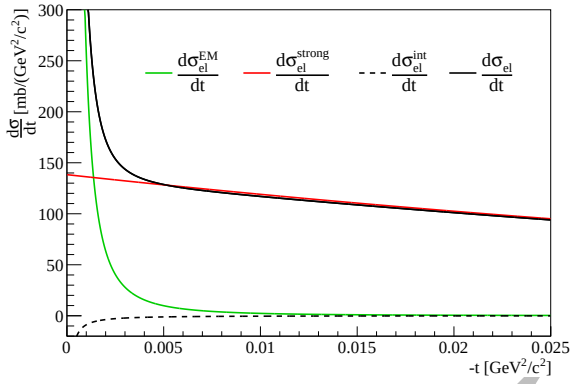

Figure 2: Contributions to the pp differential cross section $\frac{d\sigma_{el}}{dt}$ at small $|t|$.

$$\begin{aligned}\frac{\mathrm{d}\sigma}{\mathrm{d}t} &= 4\,\pi\,(\hbar c)^2\left(\frac{\alpha\,G_E^2}{t}\right)^2 \\ &+ \frac{1+\rho^2}{16\,\pi\,(\hbar c)^2}\cdot\sigma_{tot}^2\cdot e^{-B\,|t|} \\ &- (\rho+\Delta\Phi)\cdot\frac{\alpha\,G_E^2}{|t|}\cdot\sigma_{tot}\cdot e^{-\frac{1}{2}B\,|t|}\,, \end{aligned} \tag{7}$$

with α the fine structure constant, G_E the electric form factor of the proton, $\Delta\Phi$ the Coulomb phase[4], ρ the ratio of the real to imaginary part of the forward scattering amplitude, σ_{tot} the total cross section, and B the nuclear slope parameter.

The above dependence of the differential elastic cross section $d\sigma/dt$ on $|t|$ can be divided into three regions: the Coulomb region, the CNI region, and the hadronic region. At small $|t|$, the Coulomb term dominates, and $d\sigma/dt$ has a $(1/t^2)$ dependence. As $|t|$ increases, the interference between the Coulomb and hadronic contributions becomes maximal. Finally, the hadronic contribution dominates, and $d\sigma/dt$ falls off exponentially. The present status of σ_{tot} and B measurements in pp and $p\bar{p}$ collisions is shown in figures 3b and 3a, respectively [5].

In Fig. 2 we show relative values of the the three parts of the elastic pp differential cross section. One can clearly see that the dominant contribution for $-t > 0.04(\mathrm{GeV}/c)^2$, the region of this measurement, the hadronic term (the second term in this expression) is dominant.

Since the total cross section is related to the differential elastic cross section by the optical theorem Eq. 8 one can extract the total cross section σ_{tot} by extrapolating $\frac{d\sigma_{el}}{dt}$ to $t = 0$. Which is the method used in this analysis.

$$\sigma_{tot}^2 = \left(\frac{16\pi\,(\hbar c)^2}{1+\rho^2}\right)\frac{d\sigma_{el}}{dt}|_{t=0}. \tag{8}$$

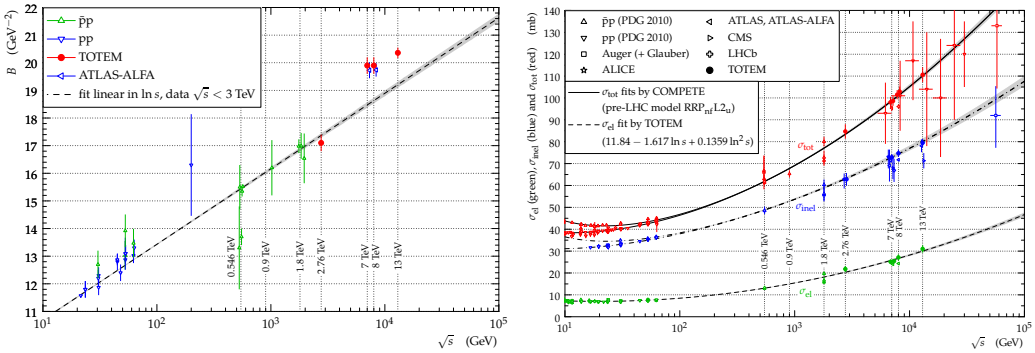

(a) The up to date compilation of the nuclear slope B for pp and $p\bar{p}$ elastic scattering as a function of *cms* energy.

(b) The up to date compilation of pp and $p\bar{p}$ total σ_{tot}, elastic σ_{el} and inelastic σ_{inel} cross-sections as a function of *cms* energy.

Figure 3: World data on B-slope and σ_{el}, σ_{tot}.

.

2 Experimental Setup

Revision : 1.25

The pp elastic scattering was measured with the Roman Pot (RP) system of the pp2pp experiment [6], which was installed at STAR for Run 15. To detect scattered forward protons the RP system was installed downstream of the STAR detector at RHIC, see Fig. 4, where the location of the Roman Pots, top view, and schematically Si detectors and scintillation counters in the Roman Pots are shown. The location between DX and D0 RHIC dipole magnets is such that no special accelerator conditions, like large β^*, are needed to operate Roman Pots together with the rest of the STAR experiment's physics program.

The two protons collide at the interaction region (IR) in a local coordinate system at a point (x_0, y_0, z_0) with respect to the reference orbit and scatter with an angle (θ_x^*, θ_y^*). The scattered protons move inside the beam pipe and are measured by telescopes of detectors placed inside Roman pots downstream of the interaction point at 15.80 and 17.60 from the IP. There is one dipole magnet (DX magnet) between the IP and the detection point. The magnet has uniform field within the acceptance of the RP system and the field magnitude is the same on both sides of the IP. The detectors are located in the vertical plane, symmetrically above and below the machine plane. The horizontal bending of DX allows decoupling between the measurement of the scattering angle, essentially given by the vertical coordinate and the measurement of the momentum, obtained from the horizontal coordinate. The DX magnet and the two Roman Pot detectors allow to measure momentum vector of the scattered protons at the detection point. Using the DX magnet, which bends the proton in the horizontal plane, one can determine the scattering angle in the (x,z) plane θ_x^* citebibi:SikoraNoteMomReconstr. The scattering angle in the (y,z) plane θ_y^* is determined from the y-coordinate measured

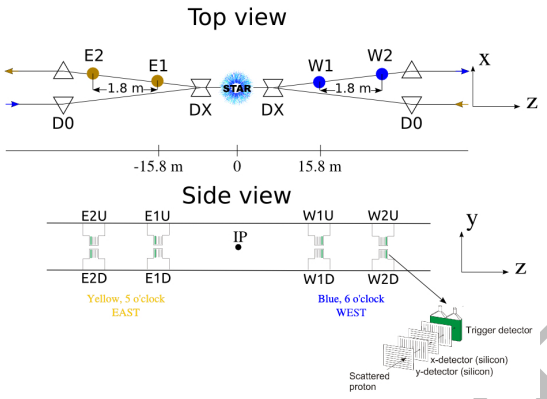

Figure 4: The layout of the RPs with the STAR detector (not to scale). The Roman Pot setup at STAR for measuring forward protons. Two sets of RPs will be positioned between DX and D0 magnets, at 15.8 m and 17.6 m from the IP. Top and side view are shown.

in the RPs.

At the location of Roman pots the vacuum pipe diameter is the limiting aperture of the scattering angle. As designed the limiting component is the inner diameter of the beam pipe inside the DX magnet and the beam pipe after the DX magnet, which has two shapes. First is a flared pipe which accommodates both incoming and outgoing beams, followed by two separate pipes for each beam.

The naming convention of the Roman Pots, detector packages and corresponding trigger counters is described in the technical note [7]. The trigger details are described in the [8]. The trigger condition was very "loose" as the trigger was considered elastic trigger (**RP_ET**) if at least one PMT on each side of the IP has a valid signal above the threshold.

$$(\mathbf{EU} \vee \mathbf{ED}) \wedge (\mathbf{WU} \vee \mathbf{WD}) \tag{9}$$

where abbreviations ***EU, ED, WU, WD*** mean that there is PMT signal in at least one of two RP stations. Letters ***E*** and ***W*** denote east and west side of interaction point (***IP***), respectively. Letters ***U*** and ***D*** stand for upper (above beam line) and down (below beam line) RP positions, respectively.

3 Data Sample

The data were acquired at the end of a store over a four hour period. The conditions were normal RHIC running, except that during that time care was taken to have multiple vernier scans done to determine the luminosity of the beams during this special data taking period. The conditions were:

1. Normal $\beta^* = 0.85m$;
2. Four hours at the end of a store to have cleanest beam possible;

3. Three special luminosity measurements to minimize systematic uncertainty on luminosity measurement;
4. Move Roman Pots as close as possible, they were moved closer than during nominal data taking.
5. Luminosity during that time was $\approx 45 \times 10^{30} cm^{-2} sec^{-1}$, see Fig. 5.

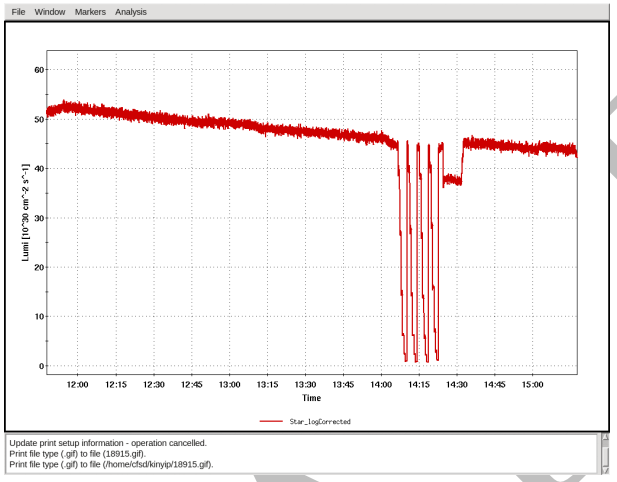

Figure 5: Luminosity for the period of data taking.

Events in initial data sample, **RP_ET** triggers, fulfill loose trigger condition (9).

However, due to the elastic scattering constraints (Fig. 6), an event is an elastic candidate if on one side of interaction point the proton is detected in the upper Roman Pots (+y) and on the other side the proton is detected in the down Roman Pots (-y). Hence, for elastic scattering event, we have two coincidence possibilities: East Up and West Down (EUWD) or East Down and West UP (EDWU). Those two cases are referred to as arm EUWD and arm EDWU. Hence strict condition for elastic scattering event candidate is:

$$(\mathbf{EU} \wedge \mathbf{WD}) \ \oplus \ (\mathbf{ED} \wedge \mathbf{WU}) \tag{10}$$

The exclusive OR requires that there are PMT signals only in one of two possible arms. Namely if there are PMT signals that form an elastic event candidate like $(EU \wedge WD)$ the event is accepted as long as there are no PMT signal in the other arm $(ED \wedge WU)$ in this case.

The sample, which fulfilled this requirement is $\approx 60\%$ of the data in initial **RP_ET** triggers fullfiling condition (9).

In order to reduce possibility that elastic scattering event is lost, due to extra background hits or PMT noise, less restrictive condition (11) was used for events that failed condition (10):

$$(\mathbf{EU} \wedge \mathbf{WD}) \ \vee \ (\mathbf{ED} \wedge \mathbf{WU}) \tag{11}$$

those events are potential candidates for elastic scatteringand and the final selection was made after clustering and point reconstruction processes.

Statistics for all used in this analysis runs is displayed in Tab. 1, where ET_{hard} is the online trigger condition 9 and ET_{accept} stands for **RP_ET** subsample of events where there were at least two reconstructed points found with pattern fullfiled condition (11).

Reconstructed points distribution of the triggered events for both arms is shown in Fig. 13. It shows shadows of the limiting aperture of DX magnet and large number hits outside of the limiting aperture which are due to elastically scattered protons passing through the magnet material (hits close to the aperture envelope), as well as physics and beam halo backgrounds.

The achieved closest distance of the first readout strip was about 30 mm or about $10\sigma_y$ of the beam, see Fig. 13, and corresponds minimum four-momentum transfer $|t_{min}| \approx 0.03$ (GeV/c)^2, see Fig.17.

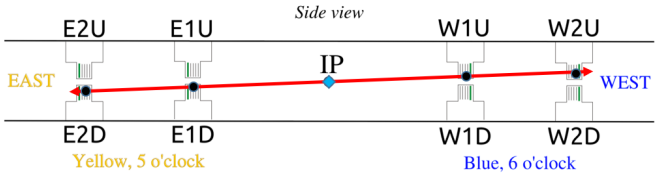

Figure 6: Elastic scattering.

Table 1: Data sample statistics used in this analysis. ET_{hard} is the online trigger condition and ET_{accept} denotes for sample of events where there were at least two reconstructed points found.

Run Number	ET_{hard}	ET_{accept}	L $[pbarn^{-1}]$	Prescale	T_{live}
16106025	575322	339421	$1.6017 \cdot 10^{-4}$	174.6077271	0.810
16106026	1842860	1108650	$5.1417 \cdot 10^{-4}$	142.7687225	0.807
16106027	1217582	743207	$3.3675 \cdot 10^{-4}$	135.8979645	0.807
16106028	1789384	1053163	$4.9260 \cdot 10^{-4}$	136.5110474	0.810
16106029	1182018	713956	$3.2354 \cdot 10^{-4}$	130.7290497	0.805
ALL	6607176	3958397	$1.8272 \cdot 10^{-3}$	-	-

4 Pedestals and noise

The pedestals and noise and signal to noise ratio study [9] was performed basing on data from pedestal runs taken regularly during Run 15. Elastic events were used to determine signal to noise ratio. The study of pedestals and noise showed that they fluctuate around 80 ADC counts and 2 ADC counts respectively. Both were stable

during the data taking period. The investigation of all strips showed that there are only two potentially hot channels out of about 20 000 (the channel number 11 and 13 of the SVX chip number 060). Those channels, however were not excluded for the analysis because they did not introduce too many extra hits in per event after more noise cuts were included in analysis.

Pedestals for silicon sensors were measured during pedestal runs performed before the beginning of each new beam fill. Based on data taken during those pedestal runs mean value and RMS of pedestals distributions for each SVX module was computed as shown in Fig. 7 and subtracted online.

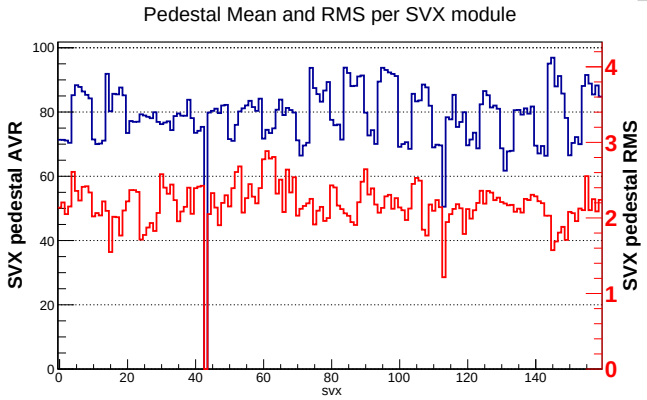

Figure 7: Average values of pedestal (blue line, left hand scale) and RMS (red line, right hand scale) for each SVX module

Distributions of ADC signal for each plane after pedestal subtraction is shown in Fig. 8. Clear Minimum Ionizing Particle (MIP) peak can be seen. For further noise suppression only channels with ADC signal greater then 3 pedestal RMS above the pedestal were passed to reconstruction - clustering procedure, see section 5.

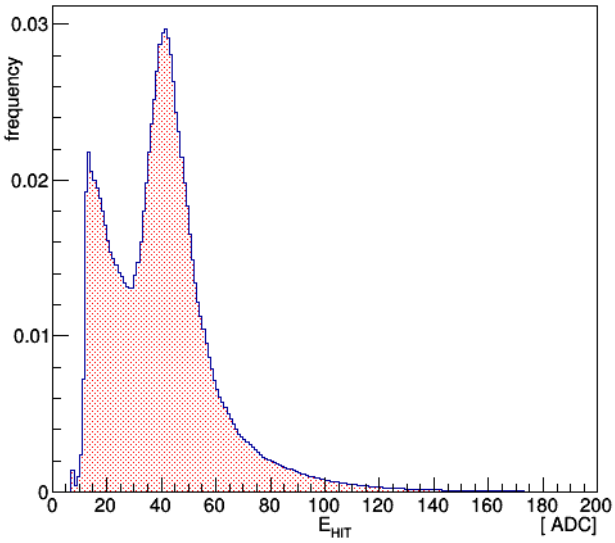

Figure 8: Hit energy distribution in ADC counts after pedestal subtraction.

5 Clustering Algorithm–Cluster Energy and Cluster Position

Revision : 1.21

Clustering procedure is performed for each detector plane separately after the noise cut of energy bigger that $3\sigma_{RMS}$ above the pedestal is applied. The procedure searches for the channel with maximum signal and continuous chain of channels adjacent to it - the set of channels found this way called cluster is removed from plane pool of hits and procedure is repeated untill there is no more hits in the plane.

In Fig. 9 We show various cluster properties for for candidate elastic events, ET events described previously. Number of clusters per plane, number of strips in a single cluster and cluster energy calculated as sum of ADC signals of channels composing cluster are shown in Fig. 9a, Fig. 9b and Fig. 9c respectively. In most cases ($\sim 95\%$) only one, as expected, cluster in a plane was found. Number of hits in a cluster (Fig. 9b) must not exceed 2 because silicon detector wafer is only $400\mu m$ thick and scattered proton trajectory perpendicular to its surface, this was found to be true for $\sim 98\%$ of reconstructed clusters. For this analysis clusters wider then 3 strips, predominantly result of background hits caused by noise or $\delta - electrons$, were not used for space point reconstruction.

Energy distribution of reconstructed clusters (Fig. 9c) is in good agreement with convoluted Landau and Gauss distributions, as expected.

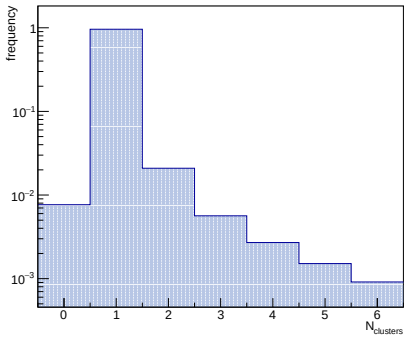

(a) Number of reconstructed clusters per plane.

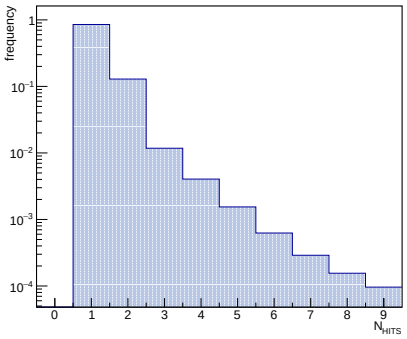

(b) Clusters width - number of strips in a cluster.

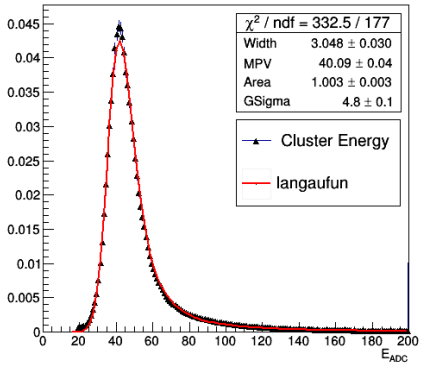

(c) Cluster energy distribution fitted with Landau-Gauss convolution.

Figure 9: a) Number of clusters per plane, b) Cluster size and c) cluster energy for reconstructed tracks (matched clusters)

.

In Fig. 10 we also show cluster energy distribution for clusters of length one, two and three strips for matched clusters from ET events.

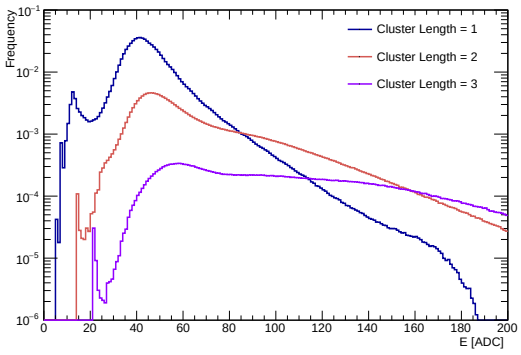

Figure 10: Cluster energy for clusters size of one, two and three strips for ET events.

Noise and cluster properties were also studied for all triggers [9]. In Fig. 11 we show cluster energy distributions for different noise cut of 4σ and 5σ, where σ denotes pedestal RMS in given silicon plane, and also cluster energy distribution after cut on minimum cluster energy of 20 ADC counts for the detector package RP E1U. The plots look very similar for all the detector packages. We conclude that there is very good separation of signal from noise and that the requirement of minimum cluster energy $E_{min} = 20$ ADC counts works well. The minimum cluster energy cut of 20 ADC is in agreement with the minimum of energy deposition for matched cluster showed in Fig. 9c, where there are no counts below ADC value smaller than 20 .

In addition to cluster energy, cluster position in local plane coordinate X_C^L is calculated as a weighted average of positions X_i of contributing strips weighted with their energy E_i. Where X_i is the strip position in the plane and the energy deposited for that strip E_i. The cluster position is then used for track reconstruction.

$$X_C^L = \frac{1.}{\sum E_i} \sum X_i E_i \tag{12}$$

The cluster position within the plane X_C^L needs to be transformed to the global coordinate system where the track are reconstructed and scattering angles are calculated. The alignment procedure of calculating offsets, which are used to obtain the cluster positions in the global coordinate system is described in the next section 8.

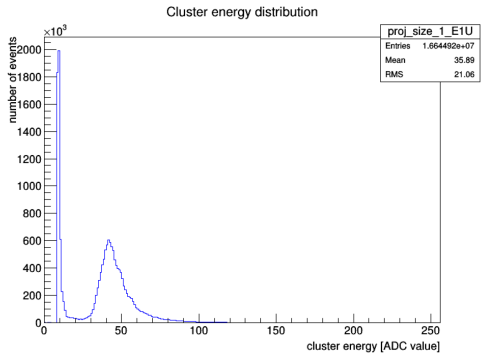

(a) Cluster energy distribution for RP E1U after 4σ cut

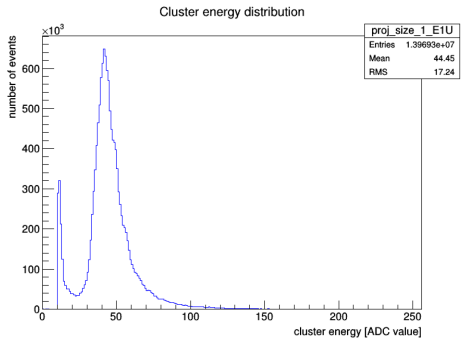

(b) Cluster energy distribution for RP E1U after 5σ cut

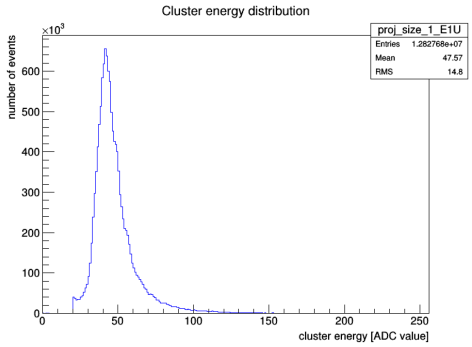

(c) Cluster energy distribution for RP E1U after $20ADC$ cut

Figure 11: Cluster energy after various cuts for RP E1U. Noise rejection is seen as function of the cut, while there is no loss in signal.

6 Point Reconstruction

Each RP station consists four silicon detector planes, two of them for X position measurement and other two for Y position. Positions of clusters found in both X or Y planes, see section 5 were compared and a pair of clusters was accepted as a point in x or y-coordinate if their positions difference Δ_X satisfied condition: $\Delta_X \leq 2 \times d_{strip} \approx 200\ \mu m$, where d_{strip} denotes strip pitch. Pairs of matched clusters found in X and Y detector planes define X and Y coordinates of space points for given RP. There may be $N_X \times N_Y$ possible cluster combinations, where N_X, N_Y are number of matched X and Y clusters, each defining a space point in a given RP: $P(X_{RP}, Y_{RP}, Z_{RP})$. In the most, $\sim 95\%$, events only one reconstructed space point in a RP vessel was found, see Fig. 12a. Position of the point is calculated as an average of the matched cluster positions. Positions of reconstructed points in each RP station for events with valid trigger pattern (10) is shown in Fig.13. One can observes large number of points beyond shadow of DX aperture limits. The efficiency for space point reconstruction for each RP was estimated basing on the data sub-sample containing only events with points reconstructed in 3 and 4 RP stations of one arm and it was calculated as the ratio of number of tracks crossing detector plane with reconstructed space point found in this palne over number of all tracks crossing the plane. Average was found to be $\approx 99\%$, and values for each RP are shown in Fig. 12c.

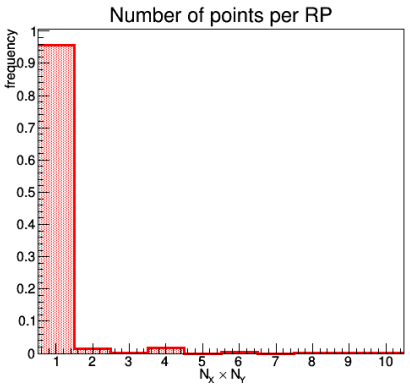

(a) Number of space points candidates per RP.

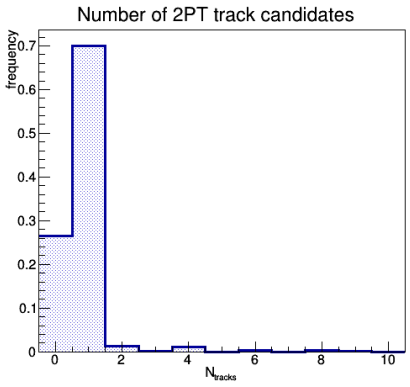

(b) Number of **2PT** track candidates on each side of the **IP**.

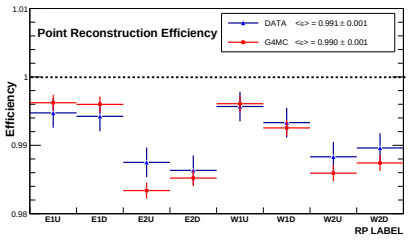

(c) Point and track reconstruction efficiency.

Figure 12: Reconstructed points and track reconstruction efficiency.

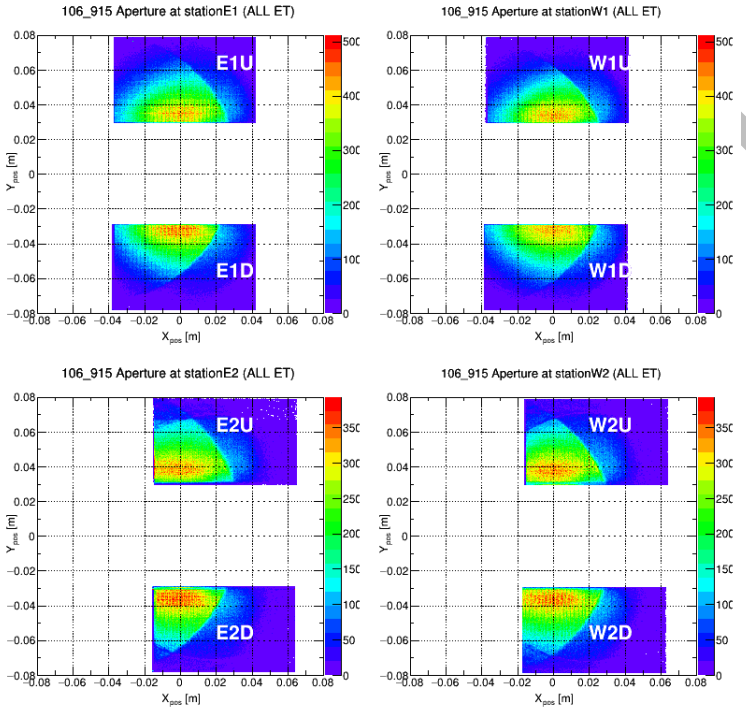

Figure 13: The (x,y) distributions of reconstructed points in Si detectors at each RP station for ET events - fulfilling condition (11).

7 Track and Scattering Angle Reconstruction

For small scattering angles θ, which are of the order of few milliardians, track-point X_{RP} and Y_{RP} positions reconstructed at given RP station can be expressed as:

$$X_{RP} = X_{IP} + \theta_X \cdot (Z_{RP} - Z_{IP}) \qquad Y_{RP} = Y_{IP} + \theta_Y \cdot (Z_{RP} - Z_{IP}) \tag{13}$$

where X_{IP}, Y_{IP}, Z_{IP} are x, y, z positions of the primary vertex, Z_{RP} is surveyed z-position (fixed for given RP) of the RP station, and θ_X, θ_Y defined as:

$$\theta_X \cong tan(\theta) \cdot cos(\phi) \;\text{ and }\; \theta_Y \cong tan(\theta) \cdot sin(\phi) \tag{14}$$

where θ and ϕ are polar and azimuth angles of scattered proton. Since the position of primary vertex is not known on event by event basis, two reconstructed points are required to calculate the scattering angle. A track is combination of two points reconstructed in two detector stations on the same side of Interaction Point (**IP**). Those points are from the two Roman Pot detectors in given arm, RP1 and RP2:

$$\theta_X = \frac{X_{RP2} - X_{RP1}}{Z_{RP2} - Z_{RP1}} \qquad \theta_Y = \frac{Y_{RP2} - Y_{RP1}}{Z_{RP2} - Z_{RP1}} \tag{15}$$

In $\sim 70\%$ events 2PT tracks were uniquely reconstructed Fig.12b. In the event with more then one track ($\lesssim 2\%$), collinearity test was used before accepting a track. The required collinearity is described in section 9. Due to geometrical acceptance of the detectors or re-scattering in dead material between the **IP** and the detection point in the RPs some of scattered protons do not pass both RP stations and only one point on the track is available. Scattering angle for this class of tracks is estimated using average vertex position, this procedure was applied in $\sim 28\%$ of events from initial elastic scattering data sample. Average position of the vertex can be estimated using data sub-sample consisting 2PT tracks. Relations (13) combined for two two points symmetrical w.r.t. IP (i.e. $Z_{RP1} = -Z_{RP2}$) lead to the formulas on middle track point (MPT) :

$$X_{MPT} \equiv (X_{RPE} + X_{RPW})/2. = X_{IP} - \theta_X \cdot Z_{IP}$$
$$Y_{MPT} \equiv (Y_{RPE} + Y_{RPW})/2. = Y_{IP} - \theta_Y \cdot Z_{IP}$$

with θ angles calculated according to (15). These relations fitted with 2-D line, provide estimate of vertex positions X_{IP}, Y_{IP} and Z_{IP}. Average values over data sample used in this analysis are:

$$< X_{IP} > = \; 0.31 \; (\pm 0.06) \; [mm]$$
$$< Y_{IP} > = \; 0.43 \; (\pm 0.03) \; [mm]$$
$$< Z_{IP} > = 53.6 \;\; (\pm 3.2) \;\; [mm]$$

Position of the vertex along Z-axis is consistent with values obtained with a different method in the Central Exclusive Production analysis, see [12].

The variable of merit, four-momentum transfer $\boldsymbol{t}$ for small angles is calculated with scttering angles $\theta_{\mathbf{X}}$ and $\theta_{\mathbf{Y}}$ (15) to a good approximation for elastic scattering as:

$$|t| = |(p_{in} - p_{out})^2| = |p^2 \cdot (cos(\theta_{IP}) - 1)| \cong p^2 \cdot \theta_{IP}^2 = p^2 \cdot (\theta_X^2 + \theta_Y^2) \tag{16}$$

8 Alignment Procedure

The alignment consists of two steps, each producing one set of offsets. In the first step survey data are utilized. The survey was done by the survey group of the accelerator department after the installation of the detector packages in the Roman Pots. This survey determined (x,y) position of the first strip in each detector package with respect to the accelerator coordinate system. That procedure is described in [10]. Cluster position in global coordinate reference system, is simply calculated by adding the offset of the first strip $\mathbf{X_0}, \mathbf{Y_0}$ f or each X and Y silicon plane, see Equation 17:

$$X_{RP} = X_0 + X_C^L \tag{17}$$

In the second step corrections to the survey alignment were obtained using reconstructed elastic events and the condition of collinearity of elastic scattering for tracks reconstructed on each side of the ***IP***. For this purpose only events with ***2PT*** tracks on both sides of ***IP*** were used, it was also required that these ***2PT*** tracks are uniquely reconstructed - one and only one reconstructed point in each RP - to assure the sample consists of cleanest ***ET*** events. In each event LSQ line fit was done through four reconstructed points. For these events, mean value of residuals for each ***RP*** station average distance of reconstructed point form fitted line $< \Delta X^{RP} >$ and $< \Delta Y^{RP} >$ was calculated as:

$$< \Delta X^{RP} > = \frac{1}{N_{events}} \sum (X_i^{RP} - X_i^{FIT})$$
$$< \Delta Y^{RP} > = \frac{1}{N_{events}} \sum (Y_i^{RP} - Y_i^{FIT})$$

where X_i^{RP}, Y_i^{RP} are reconstructed point positions and X_i^{FIT}, Y_i^{FIT} are fitted line position in the $i-th$ event. Mean residuals found this way were applied to correct first strip position in each silicon detector plane, and alignment process was then repeated with new strip positions. Typically three iterations were needed to achieve residuals distributions centered at zero - optimal relative positions between Roman Pots on opposite sides of ***IP*** in each detector arm separately. By its construction the result of the second alignment step are set of offsets in the coordinate system of the elastic scattering, where two outgoing protons are collinear.

This procedure leaves one variable unknown–the unscaterred beam trajectory and overlap with any other detector, the procedure does not assure correctness of relative position detector arm w.r.t. beam axis including potential tilt of detectors z-axis with respect to beam. Both affecting uncertainty of Monte-Carlo corrections and contributing to systematic error on reconstructed differential distribution dN/dt. The procedure was performed for each run of merit, and mean value of per run corrections - mean global correction accounting for uncertainty of detector positioning and non-scattered beam trajectory - was calculated and applied in the point/track reconstruction. Values of the corrections needed for each plane to assure co-linearity of tracks of elastically scattered protons are shown in Fig. 14.

As mentioned before, the detectors are placed downstream outgoing beam after dipole magnets ***DX***, whose uniform magnetic field is along the y-axis. The x-axis in the horizontal plane the and detector z-axis is parallel to unscaterred beam trajectory.

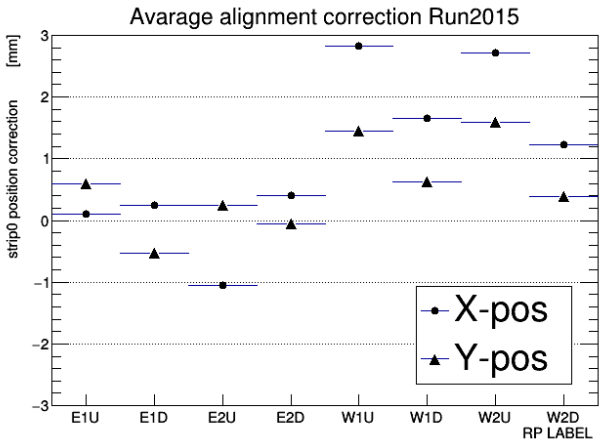

Figure 14: Alignment corrections per plane.

In that coordinate system the (x,z) plane is the bending plan. Since the magnetic field in both DX magnets are equal the bending angle of **DX** dipole on both sides of the **IP** (West and East) are equal also.

Given that, the scattering angles $\theta_X^{RP}, \theta_Y^{RP}$ measured at detector planes according to formulas in Eq. 15 become direct measurement of θ_X, θ_Y scattering angles at **IP**.

Because of the conservation of momentum the condition of collinearity for the elastic scattering event must hold, Eq 19:

$$\theta_X^W - \theta_X^E = \theta_X^{RPW} - \theta_X^{RPE} = 0 \tag{18}$$

$$\theta_Y^W - \theta_Y^E = \theta_Y^{RPW} - \theta_Y^{RPE} = 0 \tag{19}$$

Where $\theta_X^W, \theta_X^E, \theta_Y^W, \theta_Y^E$ are scattering angles at the ***IP*** and $\theta_X^{RPW}, \theta_X^{RPE}, \theta_Y^{RPW}, \theta_Y^{RPE}$ are scattering angles at the Roman Pot location.

9 Data Analysis

Revision : 1.49

In this section we describe the flow of data analysis, which has three major steps:

1. First, from the hits in Si detectors space points are reconstructed, as described in section 6.
2. Second, from the space points scattering angles θ_x in (x,z) plane and θ_y in (y,z) plane are calculated, as described in section 7.
3. Third, cuts are applied to select elastic scattering events to extract total and elastic cross sections, which is described in this section.

Given that the trigger condition was very inclusive 9, the collected data sample included in addition to elastic events the contributions from background, which consisted non elastic events and accidental coincidences of the beam halo. A series of cuts was used to select elastic events form the collected data sample. The general idea to use two types of conditions in order to minimize the previously mentioned background:

1. Collinearity condition in (θ_{West},θ_{East}) space, definition of elastic events;
2. Choice of the fiducial volume (θ, ϕ) space, to stay within clear aperture and away from the beam hallo.

The following cuts were used in selection of elastic events:

1. Choose elastic event candidates by checking the hit pattern on the East and West detectors to make sure it corresponds to the elastic event condition 10. Only events with elastic combination of reconstructed points in the the Roman Pots are accepted. Namely, combinations ($ED \wedge WU$) or ($EU \wedge WD$).
2. Only events with 2 point tracks on the East and two point tracks on the East (one track point per Roman Pot in elastic combination) are kept.
3. Since the elastic events must satisfy collinearity collinearity condition collinearity within $2\sigma_\theta$ namely $\theta_{West} - \theta_{East} < 2\sigma_\theta$, where $\sigma_\theta = 255\mu rad$, is required.
4. Finally, events within fiducial volume in (ϕ, t) space are chose

Table 2 summarizes all data analysis cuts used to reduce background and to stay within fiducial volume away from boundaries of geometrical acceptance.

Table 2: Definitions of data selection filters.

Num	Ref. Name	Description	Remark
1	***ET***	as defined in (10)	proper combination of RP points
2	***COL***	$\lvert\theta_{West} - \theta_{East}\rvert < 2\sigma_\theta$	collinearity
3	***4PT***	2PT track on both sides ***IP***	
4	***GEO***	$1.9 \leq \theta \leq 3.9$ $[mrad]$ $0.04 \leq \lvert t\rvert \leq 0.16$ $[GeV^2]$ $79.5 \leq \lvert\phi\rvert \leq 101.5$ [deg]	to stay far from edges of geometrical acceptance

In Fig. 15 we show collinearity condition $\Delta\Theta_y$ vs $\Delta\Theta_x$ with the contours of 2σ and 3σ. It is clear that the collinearity is very well satisfied for the two-point tracks.

Also the background for the collinearity was studied for various stages of analysis. The efficiency of analysis cuts is demonstrated in Fig. 16, where co-linearity distributions for reconstructed data and reconstructed Monte Carlo samples are compared for each analysis cut and estimate of background contribution is shown. Background estimate is difference between second order polynomials for data and reconstructed Monte Carlo fitted with exclusion of 5σ central region.

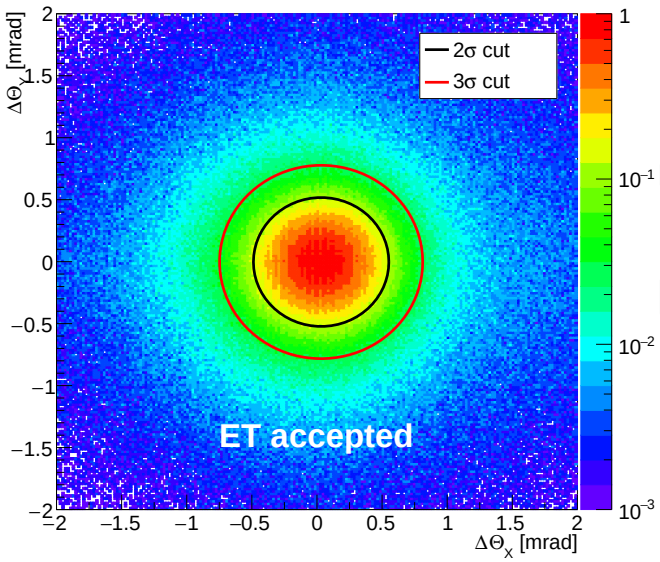

Figure 15: $\Delta\Theta_y$ vs $\Delta\Theta_x$ with the contours of 2σ and 3σ.

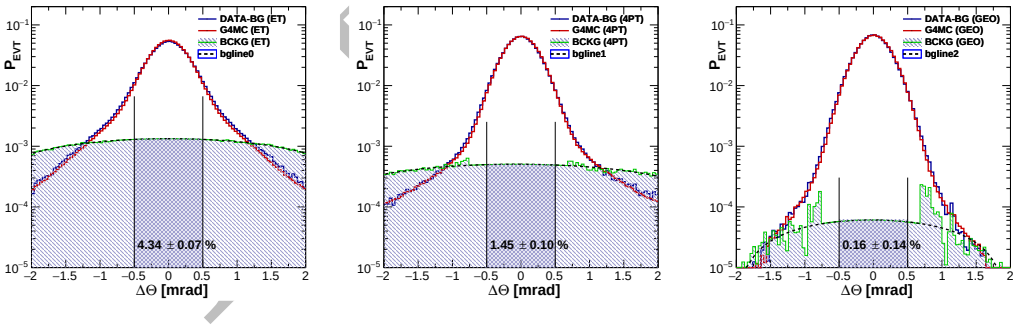

Figure 16: Co-linearity $\theta_{west} - \theta_{east}$ for ***ET, 4PT*** and ***GEO*** data sub-samples after background subtraction compared with G4MC (pure elastic scattering events only) simulated distributions. Estimated background (blue hatched area) and background remained after co-linearity cut (hatched rectangles) are shown.

The G4MC simulation, see section 10 for details, includes only background contribution from the scattered protons interacting with the material in front of the Roman Pots, like the beam pipe, magnet structure and RF shield inside the DX-D0 chamber. Hence the reduction of the background is very important by using track quality cuts and fiducial volume cuts. The ***GEO*** selection cuts results in reduction of background from ≈4.5% present in ***ET*** sample to ≈0.3%. Therefore ***GEO*** data sample is used to extract final results. In Fig. 17 the distribution of $|t|$ vs ϕ for the 4PT elastic events.

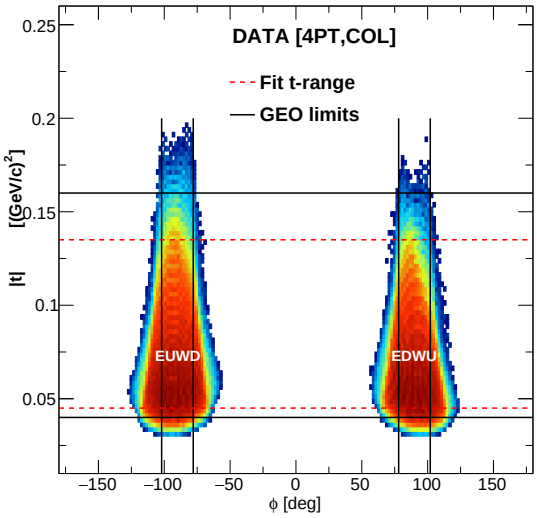

Figure 17: Four-momentm transfer $|t|$ vs ϕ distributions for data for ET 4PT collinear events.

Finally, in table 3 we show event statistics for data samples obtained after each analysis cut is applied.

Table 3: Statistics for event samples after each selection cut.

	ET	COL	4PT
ET	3.974 M	2.696 M	
4PT	1.648 M	1.306 M	
GEO	1.100 M	0.848 M	0.666 M

10 Monte Carlo Simulation

Revision : 1.19

Response of the detector was studied with Geant4 [14] based software package. It has

detailed implementation of the beam-line and Roman Pot detectors, position and read-out behavior. Physics generator used for simulation produced only elastic **pp** scattering process at energy $\sqrt{s} = 200GeV$. Kinematic range covered uniformly azimuth angle $-\pi \leq \phi \leq \pi$ and four-momentum transfer **t** within the range $0.01 \leq |\mathbf{t}| \leq 0.5$ $(\mathrm{GeV/c})^2$ distributed as $dN/dt \sim \exp(-B \cdot t)$ with $B = 15$ $(\mathrm{GeV/c})^{-2}$.

The beam parameters used in simulation:

- angular spread $\sigma_X = \sigma_Y = 180$ μrad, consistent with beam angular divergence and β^*.
- vertex position set to values estimated as described in Sec. 7 with $\sigma_{vx} = \sigma_{vy} = 0.15$ mm, consistent with beam angular divergence and β^* and $\sigma_{vz} = 500.$ mm

Hits generated in silicon detectors passed through identical as for experimental data reconstruction procedure and reconstructed MC events were filtered applying the same set of condition as in the case of data. In Fig. 18 we show comparison of the trigger patterns between GEANT4 MC and the data.

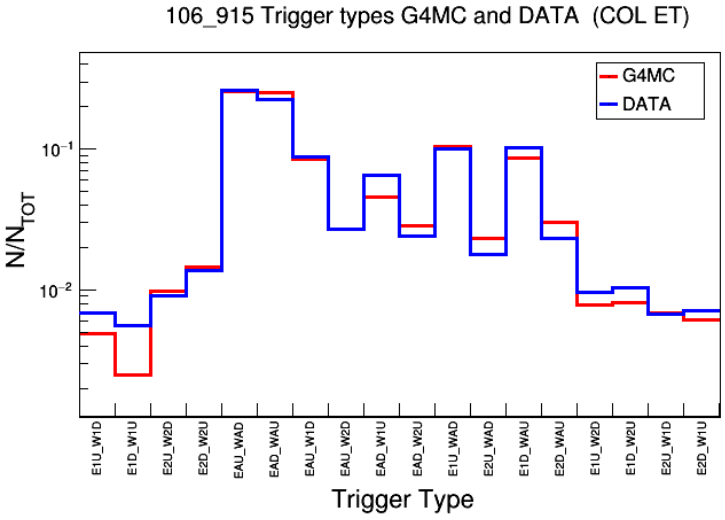

Figure 18: Comparison of trigger patterns between GEANT4 MC simulation and reconstructed DATA for ET events after co-linearity filter. Labels EAU, EAD, WAU, WAD stand for 2PT tracks found in both upper east, bottom east, upper west and bottom west RP stations, respectively

We first show hit distribution in (x,y) coordinates for various steps in analysis for reconstructed data and reconstructed G4MC full simulation and Fast Monte-Carlo (FSMC) simulation in which ET events with final state proton interacted with material on its way from IP to detector have been removed from the sample. In Fig. 19 we show reconstructed DATA and GEANT4 and FSMC simulation results at the trigger level after co-linearity filter.

In Fig. 20 we show hit distribution in (x,y) for events which have four track points for a given arm (two on each side IP).

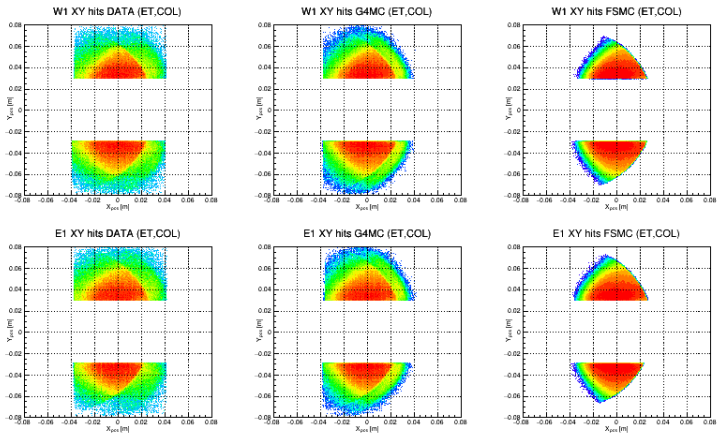

Figure 19: Hit distribution at the first RP station at the trigger level as a in (x,y) plane after colinearity filter. Reconstructed DATA (first l.h.s column) compared with G4 MC (middle column) and MC simulation where ET events with final state proton interacted with dead material on the way from IP to RP have been removed from the sample (r.h.s column).

In Fig. 21, show hit distribution in (x,y) coordinates for events which have four track points for a given arm (two on each side IP) and are within geometrical acceptance used for analysis in ϕ, t) space.

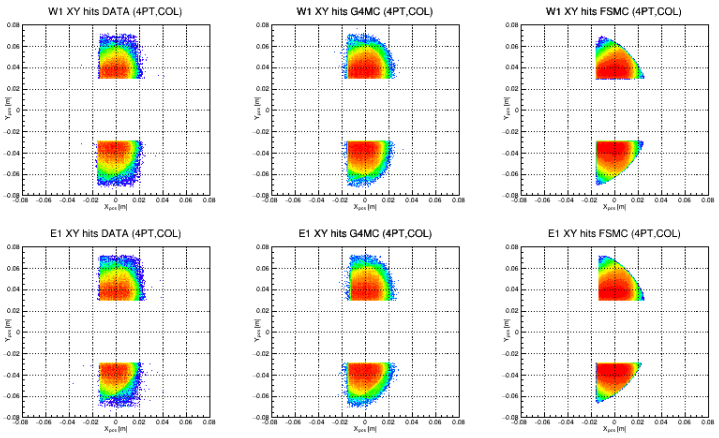

Figure 20: Hit distribution at the trigger level as a function of (x,y) after collinearity filter and for four point tracks.

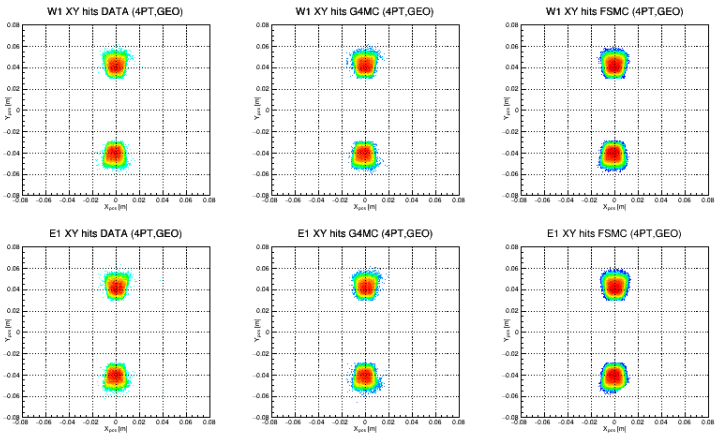

Figure 21: Hit distribution at the trigger level as a function of (x,y) after collinearity filter and for four point tracks and within geometrical acceptance used for analysis.

11 Efficiency Corrections

Revision : 1.13

The detector geometrical acceptance and limited aperture of ***DX*** magnet make that reconstructed distribution of four-momentum transfer $\boldsymbol{t}$ needs to be corrected. Differential distribution $(dN/dt)^{DATA}$ obtained from data was corrected using "bin by bin" method (aka diagonal method) with correction factors were obtained through Monte Carlo simulation (see section 10) according with formula 20, dependence of the values of correction factors on four-momentum transfer $|\boldsymbol{t}|$ for different selection filters are displeyed in Fig.22.

$$\left(\frac{dN}{dt}\right)^{DATA}_{corrected} = \left(\frac{dN}{dt}\right)^{DATA}_{reconstructed} \times \frac{(dN/dt)^{MC}_{generated}}{(dN/dt)^{MC}_{reconstructed}} \tag{20}$$

here $(dN/dt)^{MC}_{generated}$ and $(dN/dt)^{MC}_{reconstructed}$ are true MC distribution and reconstructed based on MC event sample which passed reconstruction and selection steps identical as those applied for experimental data.

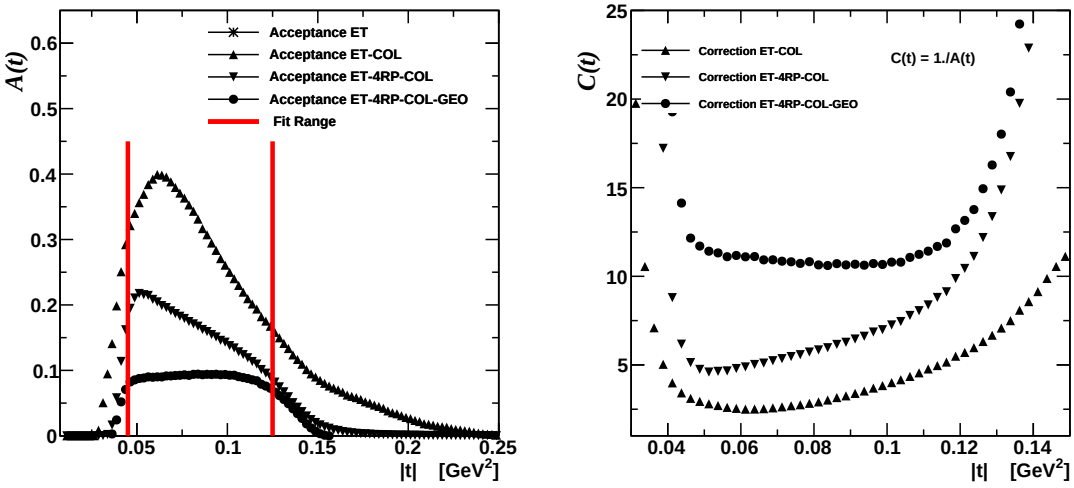

Figure 22: Comparison of acceptance ***A(t)*** (l.h.s figure) and acceptance corrections ***C(t)*** (r.h.s. figure) in fit range limits shown for data samples passed different selection filters.

12 t-distributions

Revision : 1.30

Four-momentum transfer $\boldsymbol{t}$ was calculated according to formula (16) in each detector sub-module ***EU, ED, WU, WD*** separately. Given point reconstruction and

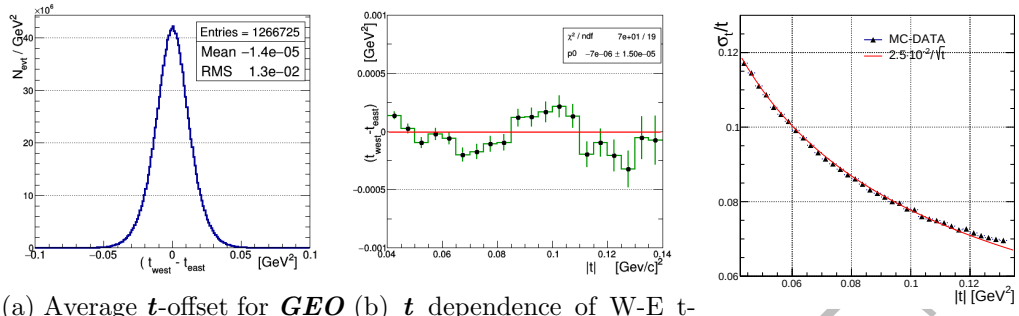

(a) Average t-offset for ***GEO*** sample. (b) t dependence of W-E t-offset. (c) t resolution.

Figure 23: The resolution σ_t/t and W-E t-offset average and dependence on t within the fit range.

alignment precision result in small differences between values of t obtained in different detector sub-modules. Offsets between t measured in West and East part of detector are shown in *Fig.*23. The offset $\Delta t \approx 2 \cdot 10^{-5}$ with $RMS \approx 0.013$ GeV^2 and value Δt varies within $\approx \pm 2.5 \cdot 10^{-4}$ GeV^2(small as compared to t bin width $2.5 \cdot 10^{-3}$ GeV^2) in the range of t used for this analysis Fig. 23b.

Four momentum-transfer resolution Δt is determined by the actual angular spread of the circulating beams, as given by the machine emittance and by the beta value at the collision point, and detector resolution. The contribution from beam angular spread :

$$\frac{\Delta t}{t} = 2p\Delta\theta/\sqrt{|t|}, \tag{21}$$

where the error on the scattering angle is due to the beam angular divergence in both (x,y) space $(\sigma_{\theta^*_x}, \sigma_{\theta^*_y})$. Since $\sigma_{\theta^*_x} = \sigma_{\theta^*_y}$ and $\theta^2 = \theta_x^2 + \theta_y^2$ we get $\Delta\theta = \sqrt{2} \cdot \sigma_{\theta^*_y}$. The values of the beam divergence for the data taking conditions were $\sigma_{\theta^*_x} = \sigma_{\theta^*_y} = 180\mu m$, hence we for the t-resolution:

$$\frac{\Delta t}{t} = 2.5 \times 10^{-2}/\sqrt{|t|} \tag{22}$$

The actual $|t|$-resolution (Fig.23c) is somewhat different as compared to formula (22 because of the effect of the beam size at the collision point, the detector resolution and Coulomb rescatterings of final state proton off the machine and the detector material, the latter contribution is seen at high $|t|$ tail. The value of the actual $|t|$-resolution staying within the range $0.5 \times 10^{-2} < \Delta t < 0.9 \times 10^{-3} GeV^2$.

Comparison of differential $d\sigma_{el}/dt$ distributions with t reconstructed with different data sub-samples is shown in Fig. 24. Residual differences are to accounted as systematic uncertainty.

Table 4: Corrected differential elastic cross-section - final sample ET-4PT-COL-GEO, where C(t) is the acceptance correction factor as shown in Fig. 22

bin	$\boldsymbol{t}$ $[GeV^2]$	$d\sigma/dt[mb/GeV^2]$	error stat	error sys	$\boldsymbol{C(t)}$
1	0.0450	69.72	±0.72	—	12.0
2	0.0475	68.13	±0.70	—	11.6
3	0.0500	65.74	±0.68	—	11.3
4	0.0525	63.23	±0.67	—	11.2
5	0.0550	60.54	±0.65	—	11.0
6	0.0575	58.76	±0.64	—	11.1
7	0.0600	57.25	±0.63	—	11.0
8	0.0625	55.42	±0.62	—	11.0
9	0.0650	53.37	±0.60	—	10.8
10	0.0675	51.67	±0.59	—	10.8
11	0.0700	49.58	±0.58	—	10.8
12	0.0725	47.61	±0.57	—	10.7
13	0.0750	46.41	±0.56	—	10.6
14	0.0775	44.59	±0.55	—	10.8
15	0.0800	43.05	±0.54	—	10.6
16	0.0825	41.58	±0.53	—	10.5
17	0.0850	40.70	±0.52	—	10.7
18	0.0875	38.50	±0.51	—	10.6
19	0.0900	37.43	±0.50	—	10.7
20	0.0925	36.11	±0.49	—	10.6
21	0.0950	34.94	±0.49	—	10.8
22	0.0975	33.69	±0.48	—	10.7
23	0.1000	32.56	±0.47	—	10.9
24	0.1025	30.51	±0.46	—	11.0
25	0.1050	30.18	±0.46	—	11.2
26	0.1075	29.15	±0.46	—	11.5
27	0.1100	28.06	±0.45	—	11.7
28	0.1125	26.96	±0.45	—	12.1
29	0.1150	25.70	±0.44	—	12.3
30	0.1175	24.94	±0.45	—	13.3
31	0.1200	23.93	±0.45	—	13.9
32	0.1225	22.43	±0.44	—	14.7
33	0.1250	21.97	±0.46	—	16.2
34	0.1275	20.96	±0.47	—	17.8
35	0.1300	20.03	±0.48	—	20.0
36	0.1325	19.25	±0.51	—	23.2
37	0.1350	19.81	±0.57	—	28.0

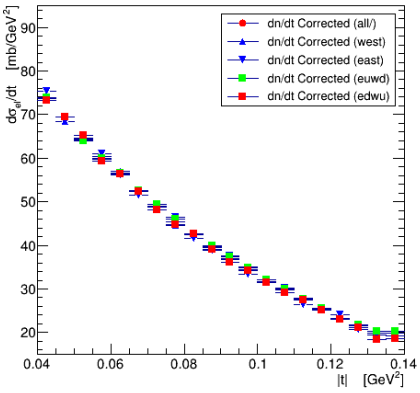

Figure 24: Corrected differential elastic distributions, with t measured separately in different data sub-samples.

13 Systematic Uncertainties

The evaluation of the systematic errors due to the uncertainty in beam emittance, vertex positions and spread, beam transport matrix elements, and incoming beam angles was based on Monte Carlo simulations. These simulations used the geometry of the experimental setup and efficiency of the detectors as an input. The largest single source of the systematic error was the uncertainty of the initial colliding beam angles.

This possible shift of the t-distribution scale was studied with the Monte Carlo simulation, using upper limits on the initial beam angle obtained from data. This resulted in an uncertainty on the fitted slope parameter of about 2%, as shown in Table 7.

Since the $|t|$ range of this measurement is far away from the CNI region, see Fig. 2, contribution from the Coulomb interaction is not necessary to consider.

Another systematic uncertainty is due to luminosity determination and estimated, see [13] to be 3.5%, relative. This is the scale uncertainty on the vertical scale of the cross section plot. Hence it does not affect the value of the slope parameter B, but introduces a corresponding systematic uncertainty on the measured cross sections: σ_{tot}, $\sigma_{elastic}$ and $\frac{d\sigma}{dt}$.

13.1 Beam Tilt

Given unknown beam position and direction relative to detector coordinate system , detector response correction function (Fig.22):

$$C(t_{rec}, t_{gen}) = \frac{(dN/dt)^{gen}}{(dN/dt)^{rec}} \tag{23}$$

was obtained from MC simulation with beam trajectory parallel to detector local coordinate z-axis. In the actual detector setup a tilt of beam axis and detector z-axis

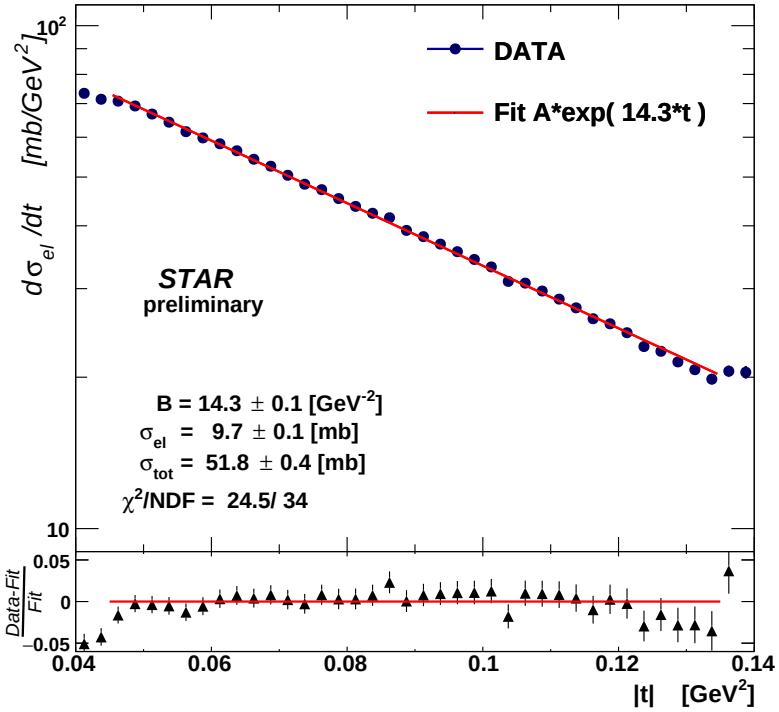

Figure 25: Corrected differential cross-section dN/dt fitted with exponential $A \cdot exp(-Bt)$.

may be present, and alignment procedure is not capable to correct for. Tilt causes an offsets τ_x and τ_y of reconstructed θ_x and θ_y angles, this leads to offset of calculated four-momentum transfer $\mathbf{t}$:

$$\mathbf{\Delta t} \simeq 2 \cdot p^2 \cdot (\theta_x \cdot \tau_x + \theta_y \cdot \tau_y) \tag{24}$$

(here terms τ_x^2 and τ_y^2 were neglected).

Presence of tilt makes MC simulated correction function inaccurate and the fit of corrected (dN/dt) distribution with expected $A \cdot exp(-B \cdot t)$ is poor. An iterative approach is made to improve fit quality by adding several values of τ_x, τ_y to reconstructed values of θ_x, θ_y and seeking for best fit probability. It is achieved for $\tau_x \approx 0.15 \cdot 10^{-3} rad$. Note weak dependence of the fit results, slope $\mathbf{B}$ and total cross-section σ_{tot} on tilts values.

$\tau_x[\mu rad]$	$\tau_y[\mu rad]$	slope **B** $[GeV^{-2}]$	σ_{tot} [mb]	σ_{el} [mb]	Probability	$\chi 2/NDF$
-200.		14.1 ±0.1	51.2 ±0.4	9.6 ±0.1	0.20	18/14
-150.		14.2 ±0.1	51.3 ±0.4	9.6 ±0.1	0.24	17/14
-100.		14.3 ±0.1	51.4 ±0.4	9.6 ±0.1	0.28	17/14
-50.		14.3 ±0.1	51.4 ±0.4	9.6 ±0.1	0.16	19/14
0.	0.	14.3 ±0.1	51.4 ±0.4	9.6 ±0.1	0.32	16/14
50.		14.3 ±0.1	51.4 ±0.4	9.6 ±0.1	0.49	13/14
100.		14.3 ±0.1	51.3 ±0.4	9.6 ±0.1	0.66	11/14
150.		14.2 ±0.1	51.3 ±0.4	9.6 ±0.1	0.81	9/14
200.		14.1 ±0.1	51.2 ±0.4	9.6 ±0.1	0.65	11/14
300.		13.9 ±0.1	50.8 ±0.4	9.7 ±0.1	0.14	20/14
	-50.	14.3 ±0.1	51.4 ±0.4	9.6 ±0.1	0.00	36/14
	-25.	14.4 ±0.1	51.5 ±0.4	9.6 ±0.1	0.09	21/14
	-15.	14.4 ±0.1	51.5 ±0.4	9.6 ±0.1	0.23	18/14
	0.	14.3 ±0.1	51.4 ±0.4	9.6 ±0.1	0.32	16/14
	15.	14.2 ±0.1	51.3 ±0.4	9.6 ±0.1	0.47	14/14
	25.	14.2 ±0.1	51.2 ±0.4	9.6 ±0.1	0.40	15/14
	50.	14.0 ±0.1	50.8 ±0.4	9.6 ±0.1	0.27	17/14
	100.	13.5 ±0.1	49.7 ±0.4	9.6 ±0.1	0.00	142/14

Table 5: Fit results, for several hypothetical tilts angle τ_x, τ_y between local detector coordinate system z-axis and beam trajectory in X-Z plane and Y-Z plane, respectively.

14 Luminosity Measurement

Revision : 1.5

The luminosity for this data set was determined with three vernier scans to minimize the systematic uncertainty. The results are described in [13]. Since at this time this work is still in progress we assume a 7% systematic uncertainty on this quantity. Based on prior experience the expected uncertainty is about 3%.

15 Total and Elastic Cross Sections

Revision : 1.17

In table 6 we show final results of the measured total cross-section, and b-slope for two different cuts to show sensitivity to the last two selection criteria. Although there is a difference, it is rather small and well within systematic uncertainties as shown the the next section. The uncertainties in table 6 are statistical only.

In Fig. 26 we also compare STAR results of B-slope 26a and of the obtained cross sections with the world data 26b. The figures are from [15].

Table 6: B slope and total cross-section obtained from fit (see *Fig.25*) in the interval $0.045 \leq |t| \leq 0.125\ GeV^2$. The uncertainties are statistical only.

FILTER	$d\sigma_{el}/dt|_{t=0}$ [mb/ GeV^2]	B $[GeV^{-2}]$	σ_{tot} [mb]	σ_{el} [mb]
4PT-COL	133.7 ±0.8	14.0 ±0.1	50.7 ±0.3	9.5 ±0.1
4PT-GEO	137.1 ±1.1	14.3 ±0.1	51.8 ±0.4	9.7 ±0.1

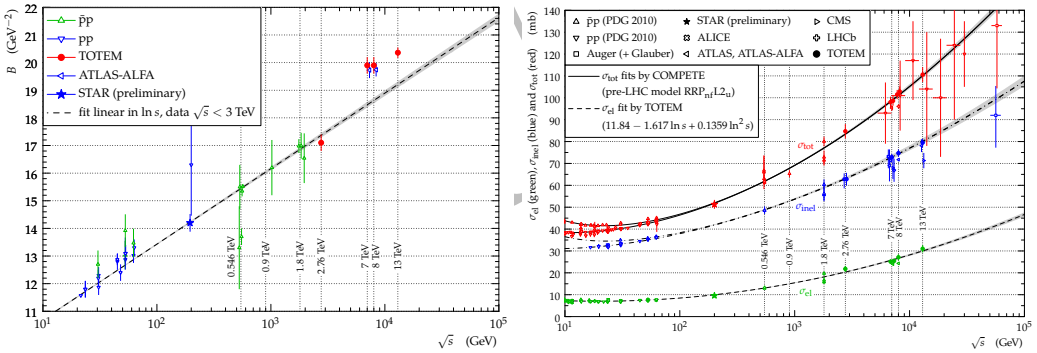

(a) Comparison of STAR result on B-slope with the world data.

(b) Comparison of STAR result on σ_{el} and σ_{tot} with the world data.

Figure 26: World data on B-slope and σ_{el}, σ_{tot}.

.

16 Summary

Revision : 1.22

At the RHIC energy of $\sqrt{s} = 200$ GeV the STAR experiment has measured differential cross-section of elastic proton–proton scattering as a function of the four-momentum transfer $\boldsymbol{t}$ in the range $0.045 < -t < 0.135\ GeV^2$. Differential elastic cross-section is well described by exponential fit with the slope $\boldsymbol{B} = 14.3 \pm 0.1(\pm 0.3)\ GeV^{-2}$, in brackets systematic uncertainty is quoted. Extrapolation of measured differential elastic cross-section over non-detected ($\approx 40\%$) low $\boldsymbol{t}$ region allowed to determine elastic cross-section to be $9.7 \pm 0.1(\pm 0.7)$ mb, and using optical theorem total $\boldsymbol{pp}$ cross-section was found to be $51.8 \pm 0.4(^{+2.1}_{-1.9})$ mb.

Table 7: Result summary with systematic uncertainties contributions.

Quantity			Statistical	Systematic uncertainties				
name	units	Value	uncertainty	$\boldsymbol{t}$-dep	norm	lumi	ρ	full
$\mathrm{d}\sigma_{el}\ /\mathrm{d}\boldsymbol{t}\|_{t=0}$	[mb/ GeV^2]	137.1	± 1.1	2.4	0.6	$^{+10.2}_{-8.9}$	n/a	$^{+10.5}_{-9.3}$
$\boldsymbol{B}$	$[GeV^{-2}]$	14.3	± 0.1	0.3	n/a	n/a	n/a	± 0.3
σ_{el}	[mb]	9.7	± 0.1	0.1	0.04	$^{+0.7}_{-0.6}$	n/a	± 0.7
σ_{tot}	[mb]	51.8	± 0.4	0.5	0.5	$^{+1.9}_{-1.7}$	$^{+0.2}_{-0.4}$	$^{+2.1}_{-1.9}$

References

[1] V. Barone, E. Predazzi, *High-Energy Particle Diffraction*, Texts and Monographs in Physics, Springer-Verlag; (2002), ISBN: 3540421076.

[2] S. Donnachie, G. Dosch, P. Landshoff, *Pomeron Physics and QCD*; Cambridge University Press; (1998), ISBN: 9780521675703.

[3] U. Amaldi et al., Phys. Lett. B43, 231 (1973).

[4] B. Z. Kopeliovich and A. V. Tarasov, Phys. Lett. B 497, 44 (2001).

[5] G. Antchev et. al, First measurement of elastic, inelastic and total cross-section at $\sqrt{s} = 13$ TeV by TOTEM and overview of cross-section data at LHC energies. TOTEM

[6] S. Bültmann *et al.*, Nucl. Instr. Meth. **A535**, 415 (2004).

[7] Rafal Sikora, Naming convention of the Roman Pot Phase II* subsystem elements. STAR Technical Note, Dec. 5, 2014Naming Convention.

[8] J.H. Lee and I. Alekseev, Trigger Definitions for RP phase-II* for Run15. STAR Technical Note, Dec. 3 2014 Run15 Trigger.

[9] M. Dobrowolska, Characterization of silicon strip detectors used in measurement of elastic proton scattering in the STAR experiment at RHIC, Bachelor of Science in Engineering Thesis, 2016. M. Dobrowolska

[10] Lukasz Fulek, Technical Note on Survey Alignment of the Silicon Strip Detectors used in the Roman Pots at STAR during RHIC 2015 Run. STAR Technical Note April 30 2018. Survey

[11] Rafal Sikora Momentum reconstruction with the Roman Pot Phase II* subsystem. STAR Technical Note, August 5 2015, Mom. Reconstr.

[12] Rafal Sikora CEP Alignment

[13] A. Drees, BNL Collider-Accelerator Department Note C-A/AP/XXX (2018). To be written

[14] S. Agostinelli *et al.*, Nucl. Instrum. Meth. A 506 (2003) 250-303

[15] Courtesy of TOTEM Experiment providing updated plots from TOTEM

[16] The COMPETE collaboration. COMPETE